

Article

Sb Nanoparticles Embedded in the N-Doped Carbon Fibers as Binder-Free Anode for Flexible Li-Ion Batteries

Xin Wang¹, Nanjun Jia¹, Jianwei Li^{1,*}, Pengbo Liu¹, Xinsheng Zhao¹, Yuxiao Lin¹, Changqing Sun² and Wei Qin^{3,*} 

¹ School of Physics and Electronic Engineering, Jiangsu Normal University, Xuzhou 221116, China

² Research Institute of Interdisciplinary Science and School of Materials Science and Engineering, Dongguan University of Technology, Dongguan 523820, China

³ College of Materials Science and Engineering, Changsha University of Science and Technology, Changsha 410114, China

* Correspondence: jwl189@163.com (J.L.); qinwei@csust.edu.cn (W.Q.)

Abstract: Antimony (Sb) is considered a promising anode for Li-ion batteries (LIBs) because of its high theoretical specific capacity and safe Li-ion insertion potential; however, the LIBs suffer from dramatic volume variation. The volume expansion results in unstable electrode/electrolyte interphase and active material exfoliation during lithiation and delithiation processes. Designing flexible free-standing electrodes can effectively inhibit the exfoliation of the electrode materials from the current collector. However, the generally adopted methods for preparing flexible free-standing electrodes are complex and high cost. To address these issues, we report the synthesis of a unique Sb nanoparticle@N-doped porous carbon fiber structure as a free-standing electrode via an electrospinning method and surface passivation. Such a hierarchical structure possesses a robust framework with rich voids and a stable solid electrolyte interphase (SEI) film, which can well accommodate the mechanical strain and avoid electrode cracks and pulverization during lithiation/delithiation processes. When evaluated as an anode for LIBs, the as-prepared nanoarchitectures exhibited a high initial reversible capacity (675 mAh g^{-1}) and good cyclability (480 mAh g^{-1} after 300 cycles at a current density of 400 mA g^{-1}), along with a superior rate capability (420 mA h g^{-1} at 1 A g^{-1}). This work could offer a simple, effective, and efficient approach to improve flexible and free-standing alloy-based anode materials for high performance Li-ion batteries.

Keywords: Sb nanoparticles; N-doped carbon fibers; free-standing anode; lithium-ion battery



Citation: Wang, X.; Jia, N.; Li, J.; Liu, P.; Zhao, X.; Lin, Y.; Sun, C.; Qin, W. Sb Nanoparticles Embedded in the N-Doped Carbon Fibers as Binder-Free Anode for Flexible Li-Ion Batteries. *Nanomaterials* **2022**, *12*, 3093. <https://doi.org/10.3390/nano12183093>

Academic Editors: Cheol-Min Park and Jiabiao Lian

Received: 11 August 2022

Accepted: 3 September 2022

Published: 6 September 2022

Publisher's Note: MDPI stays neutral with regard to jurisdictional claims in published maps and institutional affiliations.



Copyright: © 2022 by the authors. Licensee MDPI, Basel, Switzerland. This article is an open access article distributed under the terms and conditions of the Creative Commons Attribution (CC BY) license (<https://creativecommons.org/licenses/by/4.0/>).

1. Introduction

With the increasing aggravation of environmental pollution and demand for energy conversion and storage, it is critical to develop advanced energy storage devices nowadays [1]. Among the existing energy storage devices, Li-ion batteries (LIBs) have many advantages such as high energy density and high operating voltage; and are extensively used as power sources in various low power electronic devices such as mobile phones, laptops, electric bicycle, and other small power devices [2,3]. However, the commercial LIBs use graphite with low theoretical specific capacity ($372 \text{ mA} \cdot \text{h} \cdot \text{g}^{-1}$) as the anode active materials, which greatly restrict their wide application in electric vehicles and the smart-grid where high power densities are needed. Therefore, it is important to search for alternative anode materials with high specific capacity and good rate capability. So far, various kinds of anode materials such as metal materials [4–7], semimetal materials [8], transition metal oxides [9–13], metal chalcogenides and transition metal chalcogenides have been studied extensively [14–16]. Among them, Sb as a metal material is recognized as a promising anode material for LIBs because of its high theoretical specific capacity (660 mAh g^{-1}), fast charge carrier mobility, low electronegativity, decent working voltage, puckered-layer architecture and good thermodynamic properties [17]. Unfortunately, the

bulk Sb electrode is primarily hampered by its gigantic volume change (~150%) during the alloying/dealloying reaction with Li, which would cause structural pulverization, and then result in a rapid capacity fade of the cycling performance for bulk Sb anode materials [18].

It is known that nanomaterials have better mechanical properties and a larger specific area compared with those of corresponding bulk materials [19–21]. As a result, when the size of materials reduces to nanoscale, not only can the volume expansion of the active materials in the process of lithium intercalation be inhibited, but also the transmission path of the lithium ion in the electrode material may be shortened [6]. Therefore, reducing the dimension of Sb to nanoscale is an effective strategy to alleviate volume change. For example, Meng He et al. reported that monodisperse Sb nanoparticles showed good capability as anode materials in rechargeable Li-ion after 100 cycles. Nevertheless, the longer-term cycling ability is still limited due to the aggregation of Sb nanoparticles and the unstable SEI film [18]. To address these problems, different kinds of Sb/carbon composites have been synthesized. For example, Sb/carbon nanocomposites were synthesized using high energy ball milling by Glushenkov et al. [22], which exhibited a good reversible capacity of 550 mAh g⁻¹ at a current rate of 230 mA g⁻¹ after 250 cycles. Qian et al. prepared rod-like Sb/C composites by a synchronous reduction and carbon deposition process, which exhibited a reversible capacity of 478.8 mAh g⁻¹ at 100 mA·g⁻¹ after 100 cycles [23]. Thus, it is recognized that constructing Sb/C nanoscale composites can successfully improve the cycling ability of the Sb material.

Compared with 3D and 2D materials, the ionic diffusion and electronic transport length can be effectively shortened along their geometry in 1D materials, leading to fast diffusion kinetics. Electrospinning is a feasible technique to prepare various 1D carbon-containing composites. The physical and chemical properties, such as surface-to-volume ratio, mechanical strength, crystallinity, particle size and distribution of metal active materials can be tuned by using different electrospinning precursor solutions and processing parameters [24–26]. A series of anode materials have been prepared by electrospinning such as Sn/NPCFs [7], Ge/CNFs [27], Si/C@CNFs and Fe₂O₃@CNFs [9,28]. This method can also be adopted to prepare flexible and free-standing films [29,30] as working electrodes of rechargeable batteries without carbon black or binder additives [31], which could improve the volumetric energy and power density of batteries and are beneficial for the overall electrochemical performance.

Considerable efforts have been made to design highly flexible and binder-free electrodes by thermal oxidation [32], electrodeposition [33], vacuum filtration [34], self-assembly [35,36], hydrothermal method [37], and electrospinning [38,39]. However, it should be noted that forming intimate contacts between active materials and freestanding matrices via the construction of a flexible and free-standing electrode for LIBs is still a great challenge. For most freestanding electrodes, the active materials are only physically interconnected with the freestanding matrices without stable interfaces. Consequently, large stress will be generated during the repeated cycling test, resulting in poor cycling stability of the batteries. Therefore, constructing freestanding electrodes with a stable interface is important for the practical application of freestanding electrodes in flexible LIBs.

Herein, for the first time, combining the advantages of Sb nanoparticle and 1D carbon fibers, we report the synthesis of free-standing Sb nanoparticles embedded in 1D flexible N-doped carbon fibers (denoted as Sb@NCFs) using an electrospinning method for LIBs. Owing to the robust hierarchical structure and shortened Li-ion diffusion distance, the as-prepared Sb@NCFs exhibit excellent Li-ion storage performance including high specific capacity, superior rate performance and stable cycling stability.

2. Materials and Methods

2.1. Materials

Polyacrylonitrile (PAN, Mw = 1,500,000) and polyvinylpyrrolidone (PVP, Mw = 1,300,000) were purchased from Sigma-Aldrich (Shanghai) Trading Co., Ltd., Shanghai, China. Diisopropanolamine (DIPA) was purchased from Alfa Aesar (China) Chemicals Co., Ltd.,

Shanghai, China. N, N-Dimethylformamide (DMF) and antimony (III) chloride (SbCl_3) were from Sinopharm Chemical Reagent Co., Ltd., Shanghai, China. The reagents above were of analytical purity grade and used without further purification.

2.2. Synthesis of Sb@NCFs

The preparation process of Sb@NCFs is shown in Figure 1. The free-standing Sb@NCFs was synthesized by the electrospinning technique as follows: firstly, a certain amount of PAN (0.75 g) and PVP (0.25 g) were dissolved into 10 mL DMF, followed by adding 0.3 mL DIPA. The mixture above was continuously stirred for 12 h at room temperature to obtain a homogeneous solution. Subsequently, the solution was mixed with 0.7 g SbCl_3 under continuous vigorous stirring for 3 h. Lastly, the obtained precursor solution was loaded into a 20 mL plastic syringe equipped with a 21# stainless steel needle for electrospinning. A sheet of copper foil on a stainless-steel drum was used as the collector and placed 15 cm away from the tip of the stainless-steel needle. The spinning voltage, the rotating speed of the drum, and the injection flow rate were 15 kV, 60 RPM, and 0.018 mm/min, respectively. Then, the as-spun fibers were placed between the ceramic sheets and annealed at 250 °C for 2 h at a heating rate of 3 °C/min in air. Finally, the as-spun fibers were annealed at 600 °C for 2 h at a heating rate of 2 °C under N_2 atmosphere to obtain the Sb@NCFs (denoted as Sb_3). To investigate the effect of organic carbon source precursor on the electrochemical properties of Sb@NCFs , the experiment without DIPA in precursor solution was carried out and the as-synthesized sample denoted as Sb_2 , the sample synthesized without PVP and DIPA in precursor solution (1.0 g PAN) was denoted as Sb_1 .

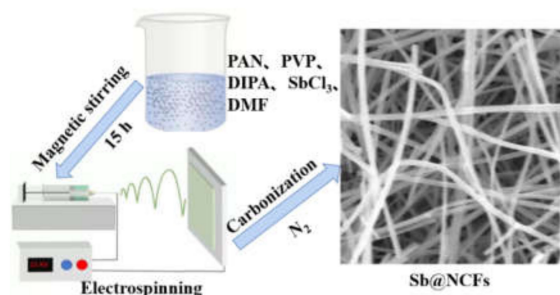


Figure 1. Synthetic illustration of the synthetic process of Sb@NCFs .

2.3. Material Characterizations

The phase and composition of Sb@NCFs were analyzed using X-ray diffraction (XRD, Bruker D8, Karlsruhe, Germany) techniques with Cu-K α radiation ($\lambda = 0.1542$ nm, $V = 40$ kV, $I = 40$ mA) at scanning rate of $0.05^\circ \text{ s}^{-1}$ in the range of $10\text{--}80^\circ$. The morphologies of the Sb@NCFs were characterized using scanning electron microscope (SEM, JSM-6510, JEOL, Tokyo, Japan) and field emission transmission electron microscopy (FETEM, Tecnai G2 20, OR, USA). X-ray photoelectron spectroscopy (XPS, Thermo ESCALAB 250XI XPS, MA, USA) was employed to analyze compositions and chemical states of the elements. The specific surface areas and pore size distributions were recorded using the Brunauer–Emmett–Teller (BET) surface area analysis (Autosorb-IQ), FL, USA. Thermogravimetric analysis (TA) was performed in air from $25\text{--}800^\circ \text{C}$ with a heating rate of $5^\circ \text{C min}^{-1}$ by using an TA thermogravimetry analyzer (Q500), Delaware, FL, USA.

2.4. Electrochemical Characterizations

The electrochemical tests were performed on CR2032 coin cells. First, the Sb@NCFs were directly cut into circular electrodes (8 mm in diameter, 0.15–0.45 mg in weight) and used as working electrode. Then, coin cells were assembled in an argon-filled glove box (MBraun, Munich, Germany), of which the working electrode, separator, counter and reference electrode were Sb@NCFs , Celgard 3501 and lithium foil with an electrolyte of 40 μL LiPF_6 in a 4:5:1 (v/v) EC/DEC/PC, respectively. After standing for 10–12 h

with the filled electrolyte, the assembled cells were connected to the Arbin battery test system (BT2000, Arbin Instruments, College Station, TX, USA). The galvanostatic discharge–charge and rate performance were conducted in the voltage range from 0.01 to 2.8 V at a room temperature. Cyclic voltammetry (CV) curves were obtained on an electrochemical workstation (CHI 760E, Shanghai, China) in the potential range of 0.01–2.8 V (vs. Li^+/Li) at a scan rate of 0.1 mV s^{-1} . The electrochemical impedance spectroscopy (EIS) was measured in the frequency range of 10^{-1} to 10^6 Hz with an AC voltage amplitude of 5 mV.

3. Results and Discussion

3.1. Characterizations of Sb@NCFs Composite

The crystal structures of the Sb_1 , Sb_2 and Sb_3 were characterized using XRD and are shown in Figure 2a. All the diffraction peaks could be indexed to Sb phase (JCPDS 35-0732) [40,41]. The main diffraction peaks of Sb located at 28.69° , 40.077° , and 41.947° corresponded to the (012), (104), and (110) planes. No impurities could be detected, which implied Sb^{3+} was reduced completely to metallic Sb by carbothermal reduction reaction [42,43]. Moreover, one could see that by adding PVP and DIPA in the precursor, Sb_3 exhibited better crystallinity than that of Sb_1 and Sb_2 .

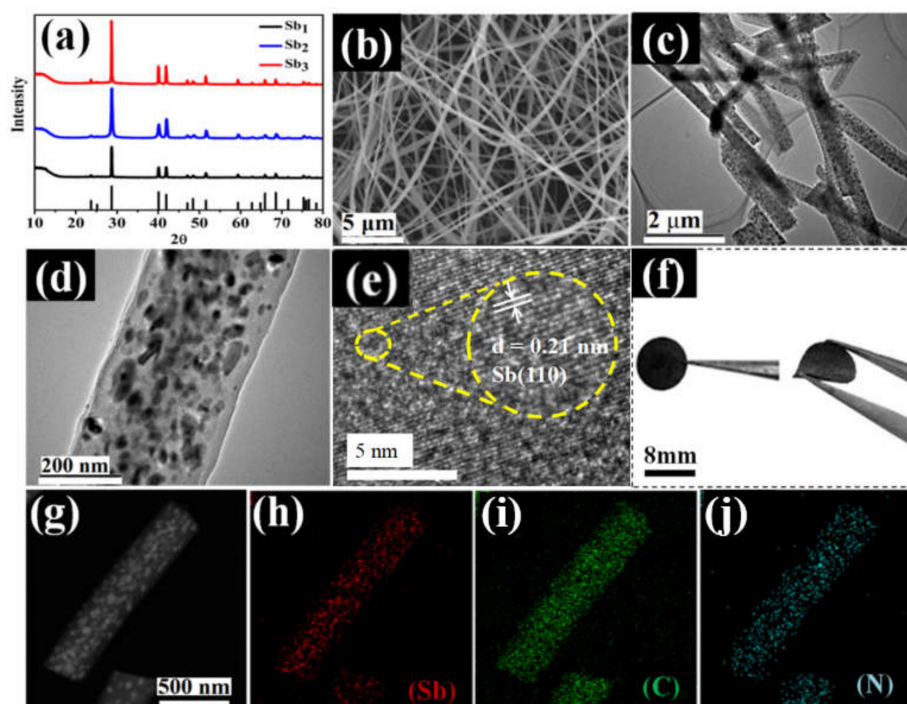


Figure 2. (a) XRD patterns of Sb_1 , Sb_2 , Sb_3 , (b) SEM images of Sb_3 , (c,d) TEM image of Sb_3 , (e) HRTEM image of Sb_3 , (f) optical images of flexible Sb@NCFs , and (g) HAADF-STEM image of Sb_3 and EDS mappings of (h) Sb, (i) C and (j) N.

To investigate the morphologies of Sb_1 , Sb_2 and Sb_3 , the SEM images are presented in Figures 2b and S1a,b. As can be seen in Figure 2b, the Sb_3 was composed of long and cross-linked fibers with smooth surfaces and with diameters ranging from 300 to 400 nm. The morphologies of Sb_2 and Sb_3 were similar to Sb_3 (Figure S1a,b). This unique one-dimensional nanostructure can facilitate the rapid transfer of electrons and Li^+ . As shown in Figure 2c–e, the TEM of Sb_3 was performed to check whether the metallic Sb had good contact with N doped carbon fibers. The TEM images displayed smooth surfaces without Sb particles, indicating that all Sb particles were encapsulated in the N-doped carbon fibers without agglomeration, which was consistent with the results of SEM. The conductive N-doped carbon coated on the outside of the metal particles not only served as a support but also suppressed the volume change during insertion/removal of lithium, further increasing

the specific capacity of the Sb_3 . The HRTEM image in Figure 2e shows the lattice fringe of 0.21 nm, which was consistent with the XRD results and corresponded to the (110) plane of Sb with hexagonal phase (JCPDS: 35-0732). To further analyze the element distribution of the Sb, C and N in the Sb_3 , EDS was carried out. As shown in Figure 2g–j, all the energy-filtered SEM maps of the Sb, C and N matched well with the SEM image, indicating that the Sb, C and N were uniformly dispersed and coexist over the entire composite. These features are beneficial to relieve volume expansion and increase electrical conductivity when used as electrode materials of batteries. The as-spun Sb@NCFs showed excellent flexibility, as demonstrated by the optical image shown in Figure 2f, which could thus be used as binder-free electrode of LIBs directly. The XPS spectra were also employed to distinguish the chemical composition and valence state of Sb_3 in Figure 3a. The peaks of Sb 3d, Sb 4d, C 1s and N 1s were observed in the survey scan spectra, indicating the coexistence of Sb, C, and N elements [44]. The C 1s spectrum is given in Figure 3b. The peaks at the binding energy of 284.6, 286.0, 287.0 and 288.2 eV were assigned to the binding energies of graphitized carbon, C–N group, C=C group, and O=C–N group bonds, respectively [45]. The peaks at the binding energy of 398.3 eV, 400.1 eV, 401.2 eV, and 402.7 eV were assigned to pyridine N, pyrrole N, quaternary N, and oxidized N (Figure 3c), respectively [46]. It is beneficial for the insertion of lithium ions because pyridine N and pyrrole N create more open channels and active sites [47]. The binding energies at 530.8 and 540.1 eV were assigned to Sb 3d_{5/2} and Sb 3d_{3/2} (Figure 3d), respectively [48]. There was a peak at ca. 199 eV, which is the fingerprint peak of Cl [49], meaning that the Cl element from SbCl_3 had been completely removed in the carbonization process.

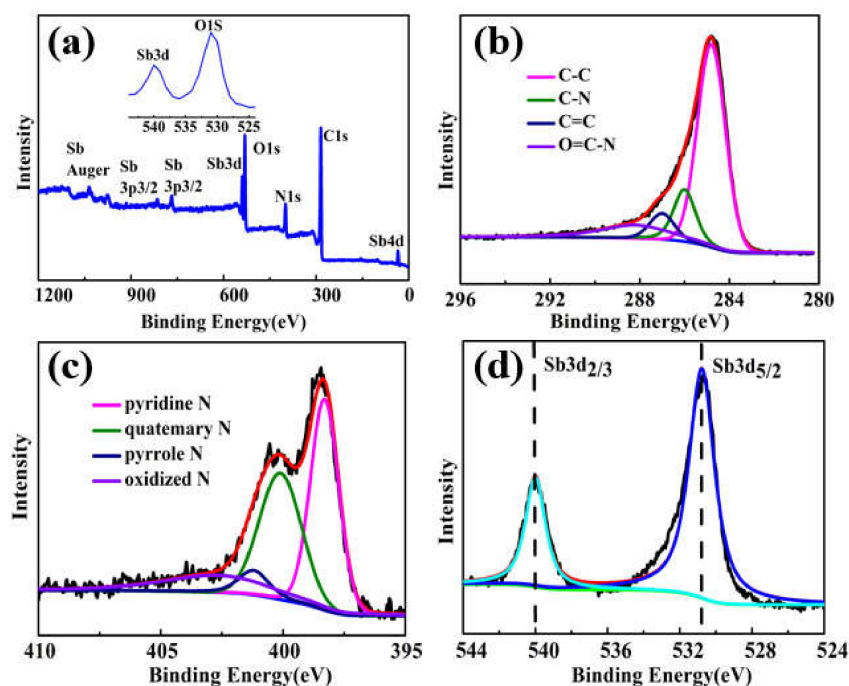


Figure 3. XPS spectra of Sb_3 : (a) survey scan, (b) C 1s, (c) N 1s, (d) Sb 3d.

The as-synthesized free-standing films were ground into powders to investigate the pore structures. The N_2 adsorption–desorption isotherms of the Sb_1 , Sb_2 and Sb_3 were carried out and are presented in Figure S2. The adsorption–desorption isotherms exhibited the characteristics of type-IV isotherm with a H_3 hysteresis loop (Figure S2a), indicating the mesoporous structure of the Sb_1 , Sb_2 and Sb_3 [41]. The specific surface areas of Sb_1 , Sb_2 , Sb_3 were 0.632, 5.193, and 24.06 $\text{m}^2 \text{g}^{-1}$, respectively. The pore-size distributions were calculated according to density functional theory and are shown in Figure S2b, indicating Sb_3 had a hierarchical porous structure with abundant mesopores and a small number of micropores centered at 1.4 nm. Correspondingly, the total pore volume of Sb_3 was 0.099 $\text{cm}^3 \text{g}^{-1}$

while those of Sb_1 and Sb_2 were only $0.022 \text{ cm}^3 \text{ g}^{-1}$ and $0.006 \text{ cm}^3 \text{ g}^{-1}$. The large specific surface area and pore volume of Sb_3 will contribute to the electrode/electrolyte contact area, providing sufficient active sites for charge transfer, shortening the diffusion length of the Li ions and finally enhancing the electrochemical performance.

The thermogravimetric (TG) curve of the Sb_1 , Sb_2 and Sb_3 (Figure S3, Supporting Information) was conducted to determine the content of Sb in the $Sb@NCFs$ composite. The slight weight loss below $300 \text{ }^\circ\text{C}$ was mainly associated with the evaporation of water absorbed on the surface of samples. The weight loss between $300 \text{ }^\circ\text{C}$ and $600 \text{ }^\circ\text{C}$ can be attributed to the burnt out of carbon and oxidation of Sb particles. The residual part of Sb_3 was around 22.9 wt.%, while Sb_2 and Sb_1 were around 15.5 wt.% and 10.7 wt.% after weight loss. The results showed that the Sb_3 had the highest Sb content of all the samples.

3.2. Electrochemical Performance of $Sb@NCFs$ Composite

The $Sb@NCF$ electrode was mechanically flexible, as shown in Figure 1f. The selected first, second, and fifth discharge/charge curves of Sb_1 , Sb_2 and Sb_3 between 0.01 and 2.8 V at a current density of 0.1 A g^{-1} are shown in Figure 4. The first discharge curve of Sb_3 (Figure 4c) showed that the voltage dropped rapidly to 0.8 V, which corresponded to the formation of the solid electrolyte interphase (SEI) on the electrode surface [42]. Then, a discernible plateau at about 0.8 V appeared which indicates the formation of a Li_3Sb phase during lithium insertion. As the voltage decreased to 0.01 V, the battery exhibited an initial specific capacity of 675.2 mAh g^{-1} , higher than the theoretical specific capacity of Sb (660 mAh g^{-1}), which could be attributed to irreversible Li ion consumption owing to the decomposition of the electrolyte and the formation of SEI films [50]. The first charge curve of Sb_3 exhibited a plateau of 1.0 V which was associated with the reversible dealloying process, with a specific capacity of 646.9 mAh g^{-1} . For Sb_2 , the first discharge/charge curves (Figure 4b) were similar to the curves of Sb_1 (Figure 4a). The initial charge and discharge specific capacities of Sb_2 and Sb_1 were 529.4, 568.7, 474.7 and 496.1 mAh g^{-1} , respectively. Compared with Sb_2 and Sb_1 , Sb_3 delivered higher specific capacities which could be ascribed to its higher specific surface area, mesoporous structure, and content of Sb.

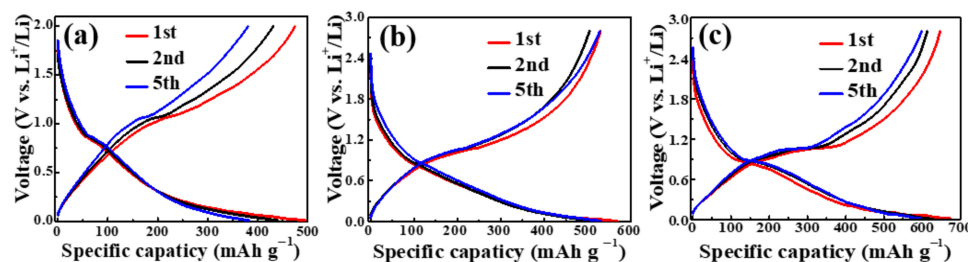


Figure 4. Galvanostatic discharge/charge curves of the 1st, 2nd, 5th cycles for (a) Sb_1 , (b) Sb_2 and (c) Sb_3 at a current density of 100 mA g^{-1} .

The initial three CV curves of Sb_3 at a scan rate of 0.1 mV s^{-1} between 0 and 2.8 V (vs. Li^+/Li) are presented in Figure 5a. In the first cathodic sweep, there was a strong cathode peak at about 0.3 V which was attributed to the formation of SEI film [6,42]. The peak did not appear in the second cycle, which reflects the high stability of the SEI film. The cathodic peak was located at 0.8 V in following cycles, which was ascribed to the reaction of metallic Sb to alloyed Li_3Sb [6]. Apart from the first cycle, the CV curves overlapped well in the following cycles, demonstrating the good electrochemical reversibility of $Sb@NCFs$ during cycling. Based on the analysis above, the electrochemical process for $Sb@NCFs$ is as follows [51]:



To further investigate the electrochemical Li-ion storage performance at high current densities, the rate capabilities of Sb_1 , Sb_2 and Sb_3 are displayed in Figure 5b. As seen,

the Sb_3 sample exhibited the reversible capacities of ca. 620, 573.9, 492.5, 459.7, 441.8 and 421.5 mAh g^{-1} at the current densities of 0.1, 0.2, 0.4, 0.6, 0.8 and 1 A g^{-1} , respectively. It was noted that the discharge capacity of Sb_3 returned to 585.3 mAh g^{-1} when the current density recovered to 0.1 A g^{-1} , suggesting that the structure of Sb_3 electrode keeps integrity after high current charge–discharge process [22,52]. The specific capacities (ca. 530.4, 456, 386.4, 344.4, 333.3, and 323.6 mAh g^{-1}) of Sb_2 at the current densities of 0.1, 0.2, 0.4, 0.6, 0.8, and 1 A g^{-1} were lower than those of Sb_3 without DIPA, owing to the smaller pore size and specific surface area. For Sb_1 without DIPA and PVP, the specific capacities (ca. 496.1, 220.6, 180.9, 149.2, 125.5, and 104.3 mAh g^{-1}) were even lower than those of Sb_2 and Sb_3 . When the current density returned to 0.1 A g^{-1} , the discharge capacity was only 460.7 mAh g^{-1} for Sb_2 and 243.1 mAh g^{-1} for Sb_1 . The cycling stability of the Sb@NCFs electrode at a current density of 0.1 and 0.4 A g^{-1} is shown in Figure 5c. The discharge capacity decayed to 629 mAh g^{-1} after the first cycle and a high reversible discharge capacity of ca. 590 mAh g^{-1} could still be retained with a high coulombic efficiency after 300 cycles. Even at a current density of 0.4 A g^{-1} , the Sb@NCFs electrode still maintained a high specific charge capacity of 480 mAh g^{-1} electrode after 300 cycles.

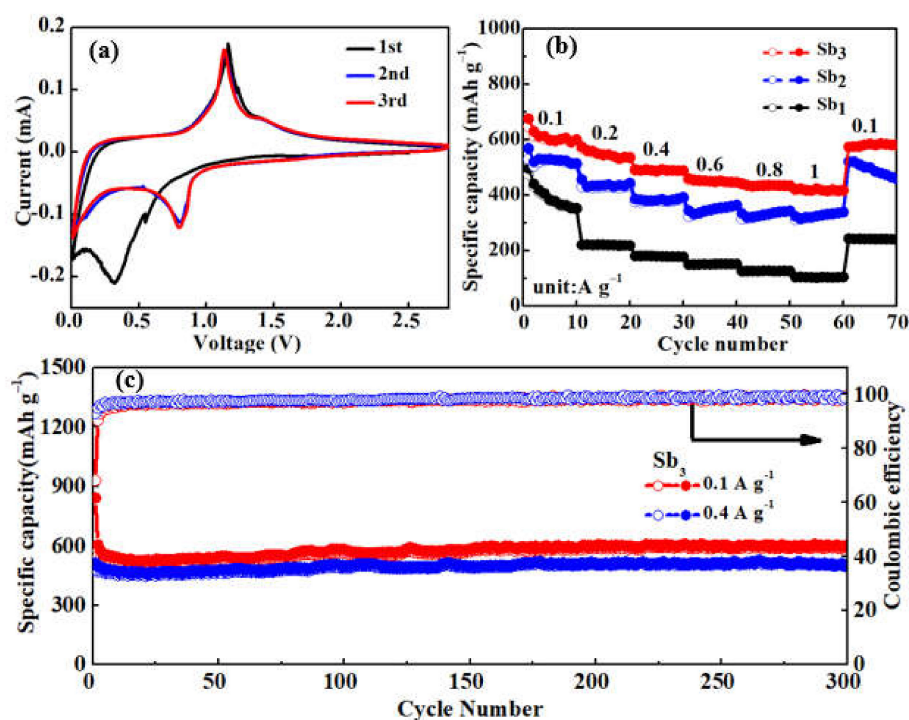


Figure 5. (a) CV curves of Sb_3 , (b) rate performances of Sb_1 , Sb_2 , Sb_3 , galvanostatic discharge–charge cycles of Sb_3 at a current density of (c) 0.1 A g^{-1} and 0.4 A g^{-1} .

To further clarify the electrochemical performance of the Sb@NCFs , EIS measurements were performed after the 10 cycles (Figure 6). All Nyquist plots can be divided into three parts, the Z' -axis intercepts, the semicircle, and the oblique line in the high and low-frequency region, which represent the resistance of electrolyte (R_e), the resistance of charge transfer (R_{ct}), and the Warburg (Z_w) impedance related to the lithium-ion diffusion (D_{Li}), respectively [23,44,53,54]. The Nyquist plots were fitted with the equivalent electric circuit and the values of the R_e , R_{ct} and Z_w are shown in the inset table of Figure 6. The diameter of the high-frequency semicircle revealed that the Sb_3 had the lowest R_{ct} value, which indicates the reduction of the unfavorable side reactions on the electrode/electrolyte interface for Sb_3 . The slope value of the low-frequency oblique line showed a trend of $\text{Sb}_3 > \text{Sb}_2 > \text{Sb}_1$, which indicated that the Sb_3 had the largest D_{Li} and fastest lithium intercalation/deintercalation, since Sb_3 had the highest conductivity and porosity. It could thus be concluded that Sb_3 had the lowest impedance (including R_e , R_{ct} , and Z_w) at the

electrode/electrolyte interface, leading to high specific capacity retention and a superior rate performance [55–58].

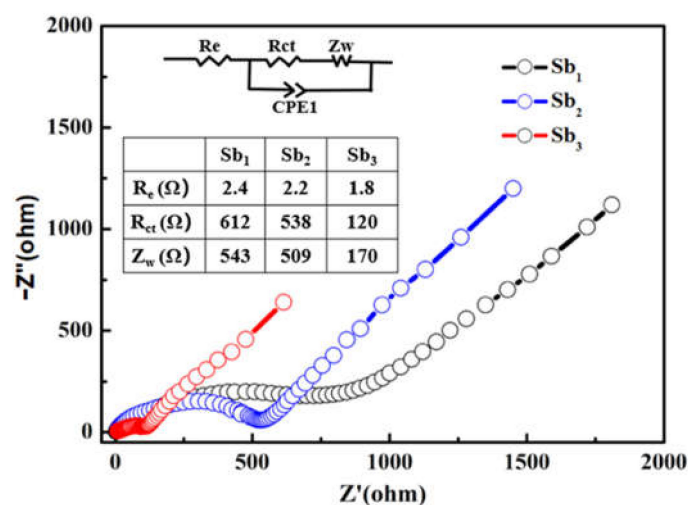


Figure 6. Nyquist plots of the Sb₁, Sb₂ and Sb₃.

Compared with the results reported in the literature, our Sb@NCF composite exhibited better electrochemical properties, as listed in Table 1 [6,22,23,42,44,52,59,60]. Considering all the above results, the Sb@NCF composite is more suitable for anode material than other developed materials for future LIBs. First, there is no need to add conductive agents, binders and collectors in the electrode preparation process. The flexible free-standing electrode is cost effective with excellent electrochemical performance. Secondly, the carbon matrix can prevent Sb nanoparticles from agglomerating into bulk particles and suppressing the volume change during repeated charging and discharging processes. Finally, the porous structure can provide rich electrolyte penetration channels and additional space to relieve structural decomposition/extraction caused by lithium-ion insertion/removal. Thus, the rate capability and cycling stability is significantly improved.

Table 1. Comparison of the electrochemical performances of the prepared Sb@NCF composites with previously reported Sb-C-based composites.

Materials	Free-Standing (Yes or No)	Current Density (A g ⁻¹)	Cycle Numbers	Capacity (mAh g ⁻¹)	References
Sb/CNT	No	0.05	30	287	[59]
Sb@C	No	0.3	20	408	[52]
Sb/C	No	0.23	250	550	[22]
		1.15	-	400	
Sb/CNT	No	0.25	50	277.4	[60]
Sb/C	No	0.1	100	315.9	[42]
		0.8	-	246.2	
Sb@C	No	0.1	100	478.8	[23]
		0.5	-	369.7	
Sb/graphite	Yes	0.1	50	424.1	[44]
		1	-	158	
Sb/C	No	0.2	100	565	[6]
		1	500	400.5	
		5	-	315.4	
Sb@NCFs	Yes	0.1	300	590	This work
		0.4	300	480	

4. Conclusions

In summary, a highly flexible Sb@NCF composite with excellent electrochemical performance was prepared by the electrospinning method. The Sb nanoparticles were uniformly dispersed in the carbon matrix which could provide a stable porous structure for the rapid charge transfer and Li-ion intercalation/deintercalation. When used as a free-standing electrode of the LIB anode, the unique Sb@NCF electrode delivered a high reversible capacity of 675 mAh g⁻¹ at the current density of 100 mA g⁻¹ and excellent capacity retention rates of 88 and 87.6% at a current density rate of 100 and 400 mA g⁻¹ after 300 cycles, respectively. The new flexible and binder-free electrode enables the practical applications of Sb-based anodes in high energy density LIBs.

Supplementary Materials: The following supporting information can be downloaded at: <https://www.mdpi.com/article/10.3390/nano12183093/s1>, Figure S1: SEM images of (a) Sb1 and (b) Sb2; Figure S2. (a) N2 adsorption-desorption isotherms and their as-calculated structural parameters in insert. (b) The pore size distribution of Sb1, Sb2, Sb3; Figure S3. TGA curves of Sb1, Sb2 and Sb3.

Author Contributions: Methodology, X.W., N.J. and J.L.; investigation and formal analysis, X.W., P.L., X.Z., Y.L. and W.Q.; writing—original draft preparation, X.W., N.J., J.L. and C.S.; writing—review and editing, N.J., J.L., W.Q. and C.S. All authors have read and agreed to the published version of the manuscript.

Funding: This research was funded by the Jiangsu Province Science and Technology Project, China (Grant No: BE2020759). Xuzhou Science and Technology Project, China (Grant No: KC19071), Natural Science Foundation of Hunan Province, China (Grant No: 2020JJ5580).

Data Availability Statement: The data presented in this study are available on request from the corresponding author.

Conflicts of Interest: The authors declare no conflict of interest. The authors claim that none of the material in our manuscript has been published or is under consideration for publication elsewhere. This manuscript is our original work.

References

1. Qin, W.; Zhou, N.; Wu, C.; Xie, M.; Sun, H.; Guo, Y.; Pan, L. Mini-review on the redox additives in aqueous electrolyte for high performance supercapacitors. *ACS Omega* **2020**, *5*, 3801–3808. [CrossRef]
2. Divakaran, A.M.; Hamilton, D.; Manjunatha, K.N.; Minakshi, M. Design, development and thermal analysis of reusable Li-ion battery module for future mobile and stationary applications. *Energies* **2020**, *13*, 1477. [CrossRef]
3. Liu, J.; Wang, M.; Wang, Q.; Zhao, X.; Song, Y.; Zhao, T.; Sun, J. Sea urchin-like Si@MnO₂@rGO as anodes for high-performance lithium-ion batteries. *Nanomaterials* **2022**, *12*, 285. [CrossRef] [PubMed]
4. Xin, F.; Whittingham, M.S. Challenges and development of tin-based anode with high volumetric capacity for Li-ion batteries. *Electrochem. Energy R.* **2020**, *3*, 643–655.
5. Gulzar, U.; Li, T.; Bai, X.; Goriparti, S.; Brescia, R.; Capiglia, C.; Zaccaria, R.P. Nitrogen-doped single walled carbon nanohorns enabling effective utilization of Ge nanocrystals for next generation lithium ion batteries. *Electrochim. Acta* **2019**, *298*, 89–96. [CrossRef]
6. Yi, Z.; Han, Q.G.; Zan, P.; Wu, Y.M.; Cheng, Y.; Wang, L.M. Sb nanoparticles encapsulated into porous carbon matrixes for high-performance lithium-ion battery anodes. *J. Power Sources* **2016**, *331*, 16–21. [CrossRef]
7. Xu, Y.; Yuan, T.; Bian, Z.; Yang, J.; Zheng, S. Tuning particle and phase formation of Sn/carbon nanofibers composite towards stable lithium-ion storage. *J. Power Sources* **2020**, *453*, 227467. [CrossRef]
8. Shi, Q.; Zhou, J.; Ullah, S.; Yang, X.; Tokarska, K.; Trzebicka, B.; Ta, H.Q.; Rummeli, M.H. A review of recent developments in Si/C composite materials for Li-ion batteries. *Energy Storage Mater.* **2021**, *34*, 735–754. [CrossRef]
9. Jayaraman, S.; Aravindan, V.; Ulaganathan, M.; Ling, W.C.; Ramakrishna, S.; Madhavi, S. Ultralong durability of porous α -Fe₂O₃ nanofibers in practical Li-ion configuration with LiMn₂O₄ cathode. *Adv. Sci.* **2015**, *2*, 1500050. [CrossRef] [PubMed]
10. Kitta, M.; Kohyama, M. Nanoscale controlled Li-insertion reaction induced by scanning electron-beam irradiation in a Li₄Ti₅O₁₂ electrode material for lithium-ion batteries. *Phys. Chem. Chem. Phys.* **2017**, *19*, 11581–11587. [CrossRef] [PubMed]
11. Hu, X.; Zeng, G.; Chen, J.; Lu, C.; Wen, Z. 3D graphene network encapsulating SnO₂ hollow spheres as a high-performance anode material for lithium-ion batteries. *J. Mater. Chem. A* **2017**, *5*, 4535–4542. [CrossRef]
12. Divakaran, A.M.; Minakshi, M.; Bahri, P.A.; Paul, S.; Kumari, P.; Divakaran, A.M.; Manjunatha, K.N. Rational design on materials for developing next generation lithium-ion secondary battery. *Prog. Solid State Chem.* **2021**, *62*, 100298. [CrossRef]

13. Solmaz, R.; Karahan, B.D. Effect of vinylene carbonate as electrolyte additive for Mn₂O₃/NiMnO₃ anodes of lithium-ion batteries. *Ionics* **2021**, *27*, 2813–2824. [[CrossRef](#)]
14. Miao, Y.E.; Huang, Y.P.; Zhang, L.; Fan, W.; Lai, F.L.; Liu, T.X. Electrospun porous carbon nanofiber@MoS₂ core/sheath fiber membranes as highly flexible and binder-free anodes for lithium-ion batteries. *Nanoscale* **2015**, *7*, 11093–11101. [[CrossRef](#)] [[PubMed](#)]
15. Lu, J.; Lian, F.; Guan, L.; Zhang, Y.; Ding, F. Adapting FeS₂ micron particles as an electrode material for lithium-ion batteries via simultaneous construction of CNT internal networks and external cages. *J. Mater. Chem. A* **2019**, *7*, 991–997. [[CrossRef](#)]
16. Xiao, X.; Ni, L.; Chen, G.; Ai, G.; Li, J.; Qiu, T.; Liu, X. Two-dimensional NiSe₂ nanosheets on carbon fiber cloth for high-performance lithium-ion batteries. *J. Alloy. Compd.* **2020**, *821*, 153218. [[CrossRef](#)]
17. Ge, X.; Liu, S.; Qiao, M.; Du, Y.; Li, Y.; Bao, J.; Zhou, X. Enabling superior electrochemical properties for highly efficient potassium storage by impregnating ultrafine Sb nanocrystals within nanochannel-containing carbon nanofibers. *Angew Chem. Int. Ed. Engl.* **2019**, *58*, 14578–14583. [[CrossRef](#)] [[PubMed](#)]
18. He, M.; Kravchyk, K.; Walter, M.; Kovalenko, M.V. Monodisperse antimony nanocrystals for high-rate Li-ion and Na-ion battery anodes: Nano versus bulk. *Nano Lett.* **2014**, *14*, 1255–1262. [[CrossRef](#)] [[PubMed](#)]
19. Zhao, Q.; Zhao, M.; Qiu, J.; Lai, W.Y.; Pang, H.; Huang, W. One dimensional silver-based nanomaterials: Preparations and electrochemical applications. *Small* **2017**, *13*, 1701091. [[CrossRef](#)]
20. David, M.E.; Ion, R.M.; Grigorescu, R.M.; Iancu, L.; Andrei, E.R. Nanomaterials used in conservation and restoration of cultural heritage: An up-to-date overview. *Materials* **2020**, *13*, 2064. [[CrossRef](#)]
21. Li, J.; Zhao, X.; Li, D.; Zheng, X.; Yang, X.; Chou, S.; Zhu, Z. Effect of size and dimensionality on the band gap and conductivity of InAs, PbS, Ge, and Bi₂S₃ nanostructured semiconductors. *Curr. Nanosci.* **2016**, *12*, 324–329. [[CrossRef](#)]
22. Ramireddy, T.; Rahman, M.M.; Xing, T.; Chen, Y.; Glushenkov, A.M. Stable anode performance of an Sb-carbon nanocomposite in lithium-ion batteries and the effect of ball milling mode in the course of its preparation. *J. Mater. Chem. A* **2014**, *2*, 4282–4291. [[CrossRef](#)]
23. Fan, L.; Zhang, J.J.; Cui, J.H.; Zhu, Y.C.; Liang, J.W.; Wang, L.L.; Qian, Y.T. Electrochemical performance of rod-like Sb-C composite as anodes for Li-ion and Na-ion batteries. *J. Mater. Chem. A* **2015**, *3*, 3276–3280. [[CrossRef](#)]
24. Zhang, L.H.; Qin, X.Y.; Zhao, S.Q.; Wang, A.; Luo, J.; Wang, Z.L.; Kang, F.Y.; Lin, Z.Q.; Li, B.H. Advanced matrixes for binder-free nanostructured electrodes in lithium-ion batteries. *Adv. Mater.* **2020**, *32*, 1908445. [[CrossRef](#)]
25. Wang, J.; Wang, Z.; Ni, J.; Li, L. Electrospun materials for batteries moving beyond lithium-ion technologies. *Electrochem. Energy R.* **2021**, *5*, 211–241. [[CrossRef](#)]
26. Li, Y.; Li, Q.; Tan, Z. A review of electrospun nanofiber-based separators for rechargeable lithium-ion batteries. *J. Power Sources* **2019**, *443*, 227262. [[CrossRef](#)]
27. Li, W.H.; Yang, Z.Z.; Cheng, J.X.; Zhong, X.W.; Gu, L.; Yu, Y. Germanium nanoparticles encapsulated in flexible carbon nanofibers as self-supported electrodes for high performance lithium-ion batteries. *Nanoscale* **2014**, *6*, 4532–4537. [[CrossRef](#)]
28. Xu, Y.; Yuan, T.; Bian, Z.H.; Sun, H.; Pang, Y.P.; Peng, C.X.; Yang, J.H.; Zheng, S.Y. Electrospun flexible Si/C@CNF nonwoven anode for high capacity and durable lithium-ion battery. *Compos. Commun.* **2019**, *11*, 1–5. [[CrossRef](#)]
29. Yang, M.; Liu, L.; Yan, H.; Zhang, W.; Su, D.; Wen, J.; Liu, W.; Yuan, Y.; Liu, J.; Wang, X. Porous nitrogen-doped Sn/C film as free-standing anodes for lithium ion batteries. *Appl. Surf. Sci.* **2021**, *551*, 149246. [[CrossRef](#)]
30. Zhang, T.; Qiu, D.; Hou, Y. Free-standing and consecutive ZnSe@carbon nanofibers architectures as ultra-long lifespan anode for flexible lithium-ion batteries. *Nano Energy* **2022**, *94*, 106909. [[CrossRef](#)]
31. Fei, L.; Williams, B.P.; Yoo, S.H.; Carlin, J.M.; Joo, Y.L. A general approach to fabricate free-standing metal sulfide@carbon nanofiber networks as lithium ion battery anodes. *Chem. Commun.* **2016**, *52*, 1501–1504. [[CrossRef](#)]
32. Xue, X.Y.; Xing, L.L.; Chen, Y.J.; Shi, S.L.; Wang, Y.G.; Wang, T.H. Synthesis and H₂S sensing properties of CuO-SnO₂ core/shell PN-junction nanorods. *J. Phys. Chem. C* **2008**, *112*, 12157–12160. [[CrossRef](#)]
33. Fu, J.Z.; Liu, H.; Liao, L.B.; Fan, P.; Wang, Z.; Wu, Y.Y.; Zhang, Z.W.; Hai, Y.; Lv, G.C.; Mei, L.F.; et al. Ultrathin Si/CNTspaper-like composite for flexible Li-ion battery anode with high volumetric capacity. *Front. Chem.* **2018**, *6*, 624. [[CrossRef](#)]
34. Köse, H.; Aydin, A.O.; Dombaycıoğlu, Ş. Graphene-based architectures of tin and zinc oxide nanocomposites for free-standing binder-free Li-ion anodes. *Int. J. Energy Res.* **2018**, *42*, 4710–4718. [[CrossRef](#)]
35. Liao, H.-S.; Lin, J.; Liu, Y.; Huang, P.; Jin, A.; Chen, X.Y. Self-assembly mechanisms of nanofibers from peptide amphiphiles in solution and on substrate surfaces. *Nanoscale* **2016**, *8*, 14814–14820. [[CrossRef](#)]
36. Rolandi, M.; Rolandi, R. Self-assembled chitin nanofibers and applications. *Adv. Colloid Interface* **2014**, *207*, 216–222. [[CrossRef](#)]
37. Jessl, S.; Copic, D.; Engelke, S.; Ahmad, S.; De Volder, M. Hydrothermal coating of patterned carbon nanotube forest for structured lithium-ion battery electrodes. *Small* **2019**, *15*, e1901201. [[CrossRef](#)] [[PubMed](#)]
38. Zhao, Y.; He, X.; Li, J.; Gao, X.; Jia, J. Porous CuO/SnO₂ composite nanofibers fabricated by electrospinning and their H₂S sensing properties. *Sens. Actuators B-Chem.* **2012**, *165*, 82–87. [[CrossRef](#)]
39. Lu, X.F.; Wang, C.; Favier, F.; Pinna, N. Electrospun nanomaterials for supercapacitor electrodes: Designed architectures and electrochemical performance. *Adv. Energy Mater.* **2017**, *7*, 1601301. [[CrossRef](#)]
40. Duan, J.; Zhang, W.; Wu, C.; Fan, Q.G.; Zhang, W.X.; Hu, X.L.; Huang, Y.H. Self-wrapped Sb/C nanocomposite as anode material for high-performance sodium-ion batteries. *Nano Energy* **2015**, *16*, 479–487. [[CrossRef](#)]

41. Zhong, L.F.; Tang, A.D.; Wen, X.; Yan, P.; Wang, J.J.; Tan, L.; Chen, J. New finding on Sb (2–3 nm) nanoparticles and carbon simultaneous anchored on the porous palygorskite with enhanced catalytic activity. *J. Alloys Compd.* **2018**, *743*, 394–402. [[CrossRef](#)]
42. Lv, H.L.; Qiu, S.; Lu, G.X.; Fu, Y.; Li, X.Y.; Hu, C.X.; Liu, J.R. Nanostructured antimony/carbon composite fibers as anode material for lithium-ion battery. *Electrochim. Acta* **2015**, *151*, 214–221. [[CrossRef](#)]
43. Zheng, J.; Yang, Y.; Fan, X.L.; Ji, G.B.; Ji, X.; Wang, H.Y.; Hou, S.; Zachariah, M.R.; Wang, C.S. Extremely stable antimony-carbon composite anodes for potassium-ion batteries. *Energ. Environ. Sci.* **2019**, *12*, 615–623. [[CrossRef](#)]
44. Yi, Z.; Han, Q.G.; Cheng, Y.; Wang, F.X.; Wu, Y.M.; Wang, L.M. A novel strategy to prepare Sb thin film sandwiched between the reduced graphene oxide and Ni foam as binder-free anode material for lithium-ion batteries. *Electrochim. Acta* **2016**, *190*, 804–810. [[CrossRef](#)]
45. Wang, M.G.; Han, J.; Hu, Y.M.; Guo, R. Mesoporous C, N-codoped TiO₂ hybrid shells with enhanced visible light photocatalytic performance. *RSC Adv.* **2017**, *7*, 15513–15520. [[CrossRef](#)]
46. Yang, F.H.; Zhang, Z.A.; Du, K.; Zhao, X.X.; Chen, W.; Lai, Y.Q.; Li, J. Dopamine derived nitrogen-doped carbon sheets as anode materials for high-performance sodium ion batteries. *Carbon* **2015**, *91*, 88–95. [[CrossRef](#)]
47. Liu, Y.C.; Zhang, N.; Jiao, L.F.; Chen, J. Tin Nanodots encapsulated in porous nitrogen-doped carbon nanofibers as a free-standing anode for advanced sodium-ion batteries. *Adv Mater.* **2015**, *27*, 6702–6707. [[CrossRef](#)]
48. Gurgul, J.; Rinke, M.T.; Schellenberg, I.; Pöttgen, R. The antimonide oxides REZnSbO and REMnSbO (RE = Ce, Pr)—An XPS study. *Solid State Sci.* **2013**, *17*, 122–127. [[CrossRef](#)]
49. Schaff, J.E.; Roberts, J.T. Adsorbed states of acetonitrile and chloroform on amorphous and crystalline ice studied with X-ray photoelectron spectroscopy. *Surf. Sci.* **1999**, *426*, 384–394. [[CrossRef](#)]
50. Wan, F.; Guo, J.Z.; Zhang, X.H.; Zhang, J.P.; Sun, H.Z.; Yan, Q.; Han, D.X.; Niu, L.; Wu, X.L. In situ binding Sb nanospheres on graphene via oxygen bonds as superior anode for ultrafast sodium-ion batteries. *ACS Appl. Mater. Interfaces* **2016**, *8*, 7790–7799. [[CrossRef](#)] [[PubMed](#)]
51. Yang, Y.C.; Yang, X.M.; Zhang, Y.; Hou, H.S.; Jing, M.J.; Zhu, Y.R.; Fang, L.B.; Chen, Q.Y.; Ji, X.B. Cathodically induced antimony for rechargeable Li-ion and Na-ion batteries: The influences of hexagonal and amorphous phase. *J. Power Sources* **2015**, *282*, 358–367. [[CrossRef](#)]
52. He, X.M.; Pu, W.H.; Wang, L.; Ren, J.G.; Jiang, C.Y.; Wan, C.R. Synthesis of nano Sb-encapsulated pyrolytic polyacrylonitrile composite for anode material in lithium secondary batteries. *Electrochim. Acta* **2007**, *52*, 3651–3653. [[CrossRef](#)]
53. Ghomi, J.S.; Akbarzadeh, Z. Ultrasonic accelerated Knoevenagel condensation by magnetically recoverable MgFe₂O₄ nanocatalyst: A rapid and green synthesis of coumarins under solvent-free conditions. *Ultrason Sonochem* **2018**, *40*, 78–83. [[CrossRef](#)] [[PubMed](#)]
54. Huang, L.; Cheng, J.L.; Li, X.D.; Yuan, D.M.; Ni, W.; Qu, G.X.; Guan, Q.; Zhang, Y.; Wang, B. Sulfur quantum dots wrapped by conductive polymer shell with internal void spaces for high-performance lithium-sulfur batteries. *J. Mater. Chem. A* **2015**, *3*, 4049–4057. [[CrossRef](#)]
55. Xu, Y.H.; Zhu, Y.J.; Liu, Y.H.; Wang, C.S. Electrochemical performance of porous carbon/tin composite anodes for sodium-ion and lithium-ion batteries. *Adv. Energy Mater.* **2013**, *3*, 128–133. [[CrossRef](#)]
56. Wu, N.T.; Zhang, Y.; Guo, Y.; Liu, S.J.; Liu, H.; Wu, H. flakelike LiCoO₂ with exposed {010} facets as a stable cathode material for highly reversible lithium storage. *ACS Appl. Mater. Interfaces* **2016**, *8*, 2723–2731. [[CrossRef](#)]
57. Wu, L.; Pei, F.; Mao, R.J.; Wu, F.Y.; Wu, Y.; Qian, J.F.; Cao, Y.L.; Ai, X.P.; Yang, H.X. SiC-Sb-C nanocomposites as high-capacity and cycling-stable anode for sodium-ion batteries. *Electrochim. Acta* **2013**, *87*, 41–45. [[CrossRef](#)]
58. Wang, H.Q.; Pan, Q.C.; Wu, Q.; Zhang, X.H.; Huang, Y.G.; Lushington, A.; Li, Q.Y.; Sun, X.L. Ultrasmall MoS₂ embedded in carbon nanosheets coated Sn/SnO_x as anode material for high-rate and long life Li-ion batteries. *J. Mater. Chem. A* **2017**, *5*, 4576–4582. [[CrossRef](#)]
59. Chen, W.X.; Lee, J.Y.; Liu, Z.L. The nanocomposites of carbon nanotube with Sb and SnSb_{0.5} as Li-ion battery anodes. *Carbon* **2003**, *41*, 959–966. [[CrossRef](#)]
60. NuLi, Y.N.; Yang, J.; Jiang, M.S. Synthesis and characterization of Sb/CNT and Bi/CNT composites as anode materials for lithium-ion batteries. *Mater. Lett.* **2008**, *62*, 2092–2095. [[CrossRef](#)]